

# Entanglement of two quantum memories via metropolitan-scale fibers

Yong Yu<sup>1,2,\*</sup>, Fei Ma<sup>1,2,3,\*</sup>, Xi-Yu Luo<sup>1,2</sup>, Bo Jing<sup>1,2</sup>, Peng-Fei Sun<sup>1,2</sup>, Ren-Zhou Fang<sup>1,2</sup>, Chao-Wei Yang<sup>1,2</sup>, Hui Liu<sup>1,2</sup>, Ming-Yang Zheng<sup>3</sup>, Xiu-Ping Xie<sup>3</sup>, Wei-Jun Zhang<sup>4</sup>, Li-Xing You<sup>4</sup>, Zhen Wang<sup>4</sup>, Teng-Yun Chen<sup>1,2</sup>, Qiang Zhang<sup>1,2,3</sup>, Xiao-Hui Bao<sup>1,2</sup>, Jian-Wei Pan<sup>1,2</sup>

<sup>1</sup>*Hefei National Laboratory for Physical Sciences at Microscale and Department of Modern Physics, University of Science and Technology of China, Hefei, Anhui 230026, China*

<sup>2</sup>*CAS Center for Excellence and Synergetic Innovation Center in Quantum Information and Quantum Physics, University of Science and Technology of China, Hefei, Anhui 230026, China*

<sup>3</sup>*Jinan Institute of Quantum Technology, Jinan, Shandong 250101, China*

<sup>4</sup>*State Key Laboratory of Functional Materials for Informatics, Shanghai Institute of Microsystem and Information Technology (SIMIT), Chinese Academy of Sciences, 865 Changning Road, Shanghai 200050, China*

*\*These two authors contributed equally to this work.*

Quantum internet will enable a number of revolutionary applications, such as distributed quantum computing, large-scale quantum communication and cooperative operation of atomic clocks. It relies on entanglement of remote quantum memories over long distances. Yet, maximal reported distance achieved so far was merely about 1 km and experimental challenges for long distance remains. Here, by using cavity enhancement to create bright atom-photon entanglement and harnessing quantum frequency conversion to shift the atomic wavelength to telecom, we create atom-atom entanglement over 22 km field-deployed fibers via two-photon interference. Moreover, by exploiting a concatenated phase-locking scheme, we use single-photon interference to entangle two atomic ensembles by transmission over 50 km coiled fibers. Our work demonstrates full-functional segments for atomic quantum networks at metropolitan scale, and pave the way towards establishing atomic entanglement over many nodes and over much longer distance in a scalable way.

Establishing remote entanglement is a central theme in quantum communication [1–3]. So far, entangled photons have been distributed over long distances both in optical fiber [4] and in free space with the assistance of satellite [5]. Despite of these remarkable progresses, the distribution only succeeds with an extremely low probability due to severe transmission losses, and photons have to be detected to verify the survival after transmission. Thus the distribution of entangled photons is not scalable to longer distances or to multiple nodes [2, 6]. A very promising solution is to prepare separate atom-photon entanglement in two remote nodes, and distribute the photons to a intermediate node for interference [7, 8]. Proper measurement of the photons will project the atoms into an remote entangled state. Although the photons still undergo transmission losses, the success of remote atomic entanglement is heralded by the measurement of photons. Therefore, if the atomic states can be stored efficiently for a considerably long duration, multiple pairs of heralded atomic entanglement can be further connected efficiently to extend entanglement to longer distances or over multiple quantum nodes through entanglement swapping [6], thus making the quantum internet based applications feasible [3, 9, 10]

Towards this goal, huge amounts of experimental investigations have been made with many different matter systems [6, 11–14]. To date, entanglement of two stationary qubits has been achieved with atomic ensembles [15–18], single atoms [19], NV centers [20–22], quantum dots [23], trapped ions [24, 25] etc. Nevertheless, for

all systems, the maximal entanglement distance achieved so far was merely 1.3 km [21]. To extend the distance into metropolitan scale, there are three main experimental challenges, to achieve bright matter-photon entanglement, to reduce the transmission losses, and to realize stable and high-visibility interference in field fibers. In this paper we combine the atomic ensemble based quantum memory with efficient quantum frequency conversion (QFC) [26], and we realize the entanglement of two quantum memories via fiber transmission over dozens of kilometers. We make use of cavity enhancement to create a bright source of atom-photon entanglement. We employ the differential-frequency generation (DFG) process in a periodically-poled lithium niobate (PPLN) waveguide chip to shift the single-photon wavelength from near infrared to telecom O band for low-loss transmission in optical fibers. We then make use of a two-photon interference scheme [8, 27] to entangle two atomic ensembles over 22 km field-deployed fibers. Moreover, we make use of a single-photon interference scheme [7] to entangle two atomic ensembles over 50 km coiled fibers. Our work demonstrates the full-functional segments for atomic quantum networks and quantum repeater [28], and is soon to enable repeater-based quantum communications, and paves the way towards building large-scale quantum networks over long distances in a scalable way in the near future [1, 3].

## Quantum memory with telecom interface

Our experiment consists of two similar nodes linked

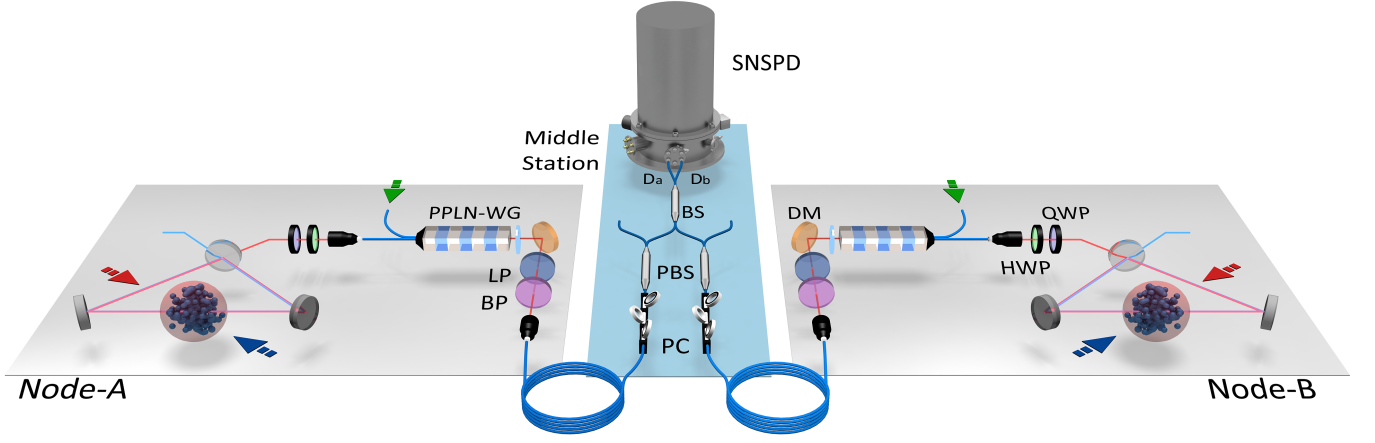


FIG. 1. **Schematic of the remote entanglement generation between atomic ensembles.** Two remote quantum memory nodes are linked by a fiber channel and a middle station for photon measurement. In Node-A (B), a  $^{87}\text{Rb}$  atomic ensemble is put inside a ring cavity. All atoms are prepared in the ground state at first. We first create a local entanglement between atomic ensemble and a write photon by applying a write pulse (blue arrow). Then the write-out photon is collected along clockwise (anticlockwise) cavity mode and by sent to the QFC module. With the help of a PPLN waveguide chip (PPLN-WG) and a 1950 nm pump laser (green arrow), 795 nm write-out photon is converted to telecom O band. The combination of a half-wave-plate (HWP) and a quarter-wave-plate (QWP) helps write-out photon coupling to the TM-polarized mode of the waveguide efficiently. After noise filtering, two write-out photons are transmitted through long fibers, interfering in a BS and detected by two SNSPDs with efficiencies of about 50% at dark count rate of 100Hz. The effective interference in the middle station heralds two ensembles entangled. Fiber polarization controllers (PCs) and polarization beamsplitters (PBSs) before the interference BS is designed for actively compensating polarization shift in the long fiber. To retrieve the atom state, we apply a read pulse (red arrow) counter-propagate to the write pulse. With the help of phase match of spin-wave and cavity enhancement, the atomic state is retrieved efficiently into anticlockwise (clockwise) mode of ring cavity.

via long-distance fibers, as shown in Fig. 1. In each node, an ensemble of  $\sim 10^8$  atoms trapped and cooled by laser beams serves as the quantum memory [6]. All atoms are initially prepared in the ground state  $|g\rangle$ . Following the Duan-Lukin-Cirac-Zoller (DLCZ) protocol [7], in each trial, a weak write pulse coupling ground state atoms to the excited state  $|e\rangle$  induces a spontaneous Raman scattered write-out photon together with a collective excitation of the atomic ensemble in a stable state  $|s\rangle$  with a small probability  $\chi$ . The collective excitation can be stored for long duration and later retrieved on demand as a read-out photon in a phase-matching mode by applying the read pulse which couples the transition of  $|s\rangle \leftrightarrow |e\rangle$ . The write-out and the read-out photons are nonclassically correlated. By employing a second Raman scattering channel  $|g\rangle \rightarrow |e\rangle \rightarrow |s'\rangle$ , we can create the entanglement between polarization of the write-out photon and internal state of the atomic ensemble [29]. To further enhance the readout efficiency and suppress noise from control beams, we build a ring cavity with a finesse of  $F = 23.5$  around the atomic ensemble. The ring cavity not only enhances the retrieval but also serves as a filter to eliminate the necessity of using external frequency filters to suppress noise [30]. Typically, the overall efficiency of detecting a readout photon conditioned on a detected write-out photon is about 35%.

To create remote atomic entanglement over a long distance, it is crucial that the photons are suitable for

low-loss transmission in optical fibers. Thus we shift wavelength of the write-out photon from near infrared (3.5 dB/km at 795 nm) to telecom O band (0.3 dB/km at 1342 nm) via the DFG process. We make use of reverse-proton-exchange PPLN waveguide chips. Optimal coupling efficiency and transmission for 795 nm signal and 1950 nm pump are simultaneously achieved in one chip by an integrated structure consisting two waveguides (see Fig. 4b and Supplementary Information). Fig. 2a shows its overall conversion efficiency up to  $\eta_{conv} \approx 70\%$  with 270 mW pump laser. Under this pump power, there are three main spectral components of noise: 1950 nm, 975 nm and 650 nm, which come from pump laser and its second and third harmonic generation. They are all spectrally far enough away from 1342 nm and thus can be cut off via the combination of two dichroic mirrors and a long-pass filter edged at 1150 nm. The pump laser also induces broadband Raman noise, the spectral brightness of which around 1342 nm is measured to be  $\sim 500$  Hz/nm. Thus, we use a bandpass filter (centred at 1342 nm, 5 nm linewidth) to confine this noise to  $\sim 2.5$  kHz, which corresponds to a signal-to-noise ratio of  $\text{SNR} > 20 : 1$  as depicted in Fig. 2a. The filtering process induces only 20% loss, and fiber coupling brings another 40% loss. The end-to-end efficiency of our QFC module is  $\eta_{QFC} = 33\%$ , which is the highest value for all memory-telecom quantum interfaces [31–37] reported so far to the best of our knowledge. In addition, we perform a Hanbury-Brown-

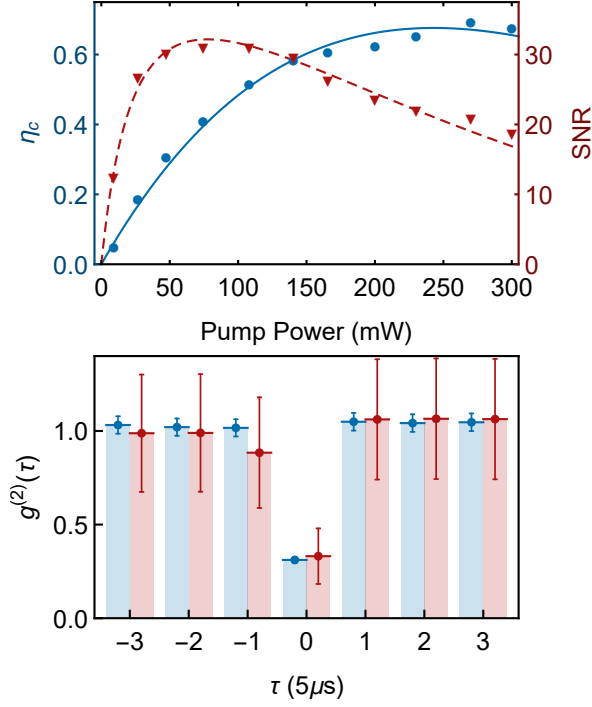


FIG. 2. **Performance of the telecom interface.** **a**, The conversion efficiency  $\eta_{conv}$  and SNR varies as a function of pump laser power. Blue dots refers to the overall conversion efficiency of the PPLN waveguide chip, red triangles refers to SNR compared with  $\chi \cdot \eta_{conv}$  ( $\chi = 0.015$ ). **b**, Results of the Hanbury-Brown-Twiss experiment with (red) and without (blue) QFC. The write-out photons are measured conditionally on the detection of a corresponding read-out photon.

Twiss experiment for the write-out photons with and without QFC, with the results shown in Fig. 2b, which verifies that the single-photon quality is well preserved during QFC.

### Entanglement over 22 km field fibers

We first perform a two-node experiment via two-photon interference (TPI) [18, 27]. In each node, we create entanglement between polarization of the write-out photon and internal state of the collective excitation [29, 30]. The entangled state can be expressed as  $(|\uparrow\odot\rangle + |\downarrow\odot\rangle)/\sqrt{2}$ , where  $|\uparrow\rangle$  or  $|\downarrow\rangle$  denotes an atomic excitation in  $|s\rangle$  or  $|s'\rangle$  respectively, and  $|\odot\rangle$  and  $|\odot\rangle$  denote polarization of the write-out photon. To characterize the atom-photon entanglement, we perform quantum state tomography, with the result shown in Fig. 3. We get a fidelity of  $0.932 \pm 0.040$  for node A and  $0.934 \pm 0.038$  for node B when  $\chi = 0.019$ . The two nodes locate in one lab in USTC east campus (N 31°50'6.96'', E 117°15'52.07'') as shown in Fig. 4a. Once the polarization entanglement is ready, the write-out photon is converted by QFC into telecom band locally. Two photons from different nodes are transmitted along two parallel field-deployed

commercial fiber channels (11km/channel) from USTC to Hefei Software Park (N 31°51'6.01'', E 117°11'54.72'') as shown in Fig. 4a. Over there, we perform a Bell-state measurement (BSM) by detecting two photons simultaneously with superconducting nanowire single photon detectors (SNSPDs). A successful BSM result heraldedly projects the two atomic ensembles into a maximally entangled state

$$|\Psi_s^\pm\rangle_{AB} = \frac{1}{\sqrt{2}}(|\uparrow\downarrow\rangle \pm |\downarrow\uparrow\rangle), \quad (1)$$

with a internal sign determined by the result of BSM.

Strong polarization dependence of DFG in PPLN waveguide makes it difficult to perform QFC directly for a polarization encoded photon. In this experiment, we transform the polarization encoding into time-bin encoding and let the two photonic modes pass through the QFC module in sequence with the same polarization. The transformation is realized through an asymmetric Mach-Zender interferometer (AMZI) as shown in Fig. 4b. A fast Pockels cell is employed to actively switch the polarizations into uniform. For time-bin encoding, it is crucial that the two modes have a stable relative phase shift, which is realized via active stabilization of the two AMZIs (see Methods). Moreover, the transformation into time-bin encoding offers additional advantage of robustness in long-distance transmission in fibers.

Before long-fiber experiments, we characterize the atom-atom entanglement locally without QFC. For the measurement of the atomic qubits, we first apply Raman rotations [38], later retrieve the excitations into read-out photons and make polarization measurement [30]. Measurement in arbitrary basis is realized via configuring the Raman pulses. Fig. 5a shows the fidelity variation versus  $\chi$  and we get  $\mathcal{F} = 0.842 \pm 0.080$  at the best working point. This is in good agreement with theoretical simulations (see Supplementary Information). Furthermore, the fidelity is basically invariant along with  $\chi$  after subtracting the accidental coincidences. This implies the main source of infidelity is high-order excitations in the Raman scattering process.

The field-deployed long fiber (L=22 km) induces 8 dB of attenuation. Besides, the long fiber leads to random rotations of polarization. To optimize the indistinguishability, we apply polarization filtering for the photons before interference. In addition, we perform actively polarization compensation to ensure a high filtering efficiency and get an average efficiency of 98% as shown in Fig. 4c. To reduce the background noise in the fiber channels, we carefully shade all the fusion points and get an average background noise  $\sim 280$  Hz (including dark counts of the detector). In the long fiber case, to increase entangling rate, we set the excitation probability to be  $\chi = 0.038$ . The measured visibility for the atom-atom entanglement in the  $|\uparrow\rangle/|\downarrow\rangle$  basis is  $V_1 = 0.630 \pm 0.073$ . Adjusting Raman pulse delay  $\delta t$ , we could observe a sinusoidal oscillation in the  $|\uparrow\rangle \pm |\downarrow\rangle$  basis as shown in Fig. 5b with a visibility of  $V_2 = 0.612 \pm 0.004$ . Thus the entanglement fidelity

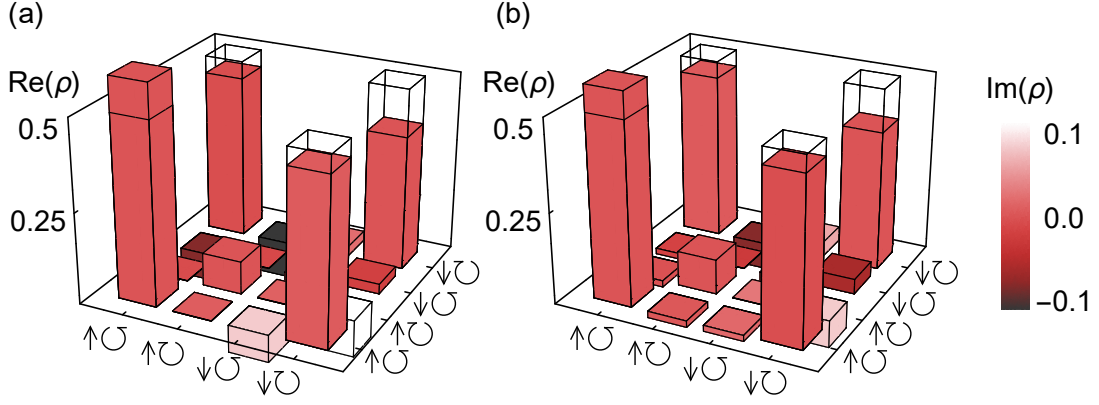


FIG. 3. **Tomography of the atom-photon entanglement.** **a, b,** The reconstructed density matrix between write-out photon and atomic spin-wave in Node-A (**a**) and B (**b**). In each element of the matrix, the height of the bar represents its real part and the color represents its imaginary part. The transparent bars indicate the ideal density matrix of the maximally entangled state.

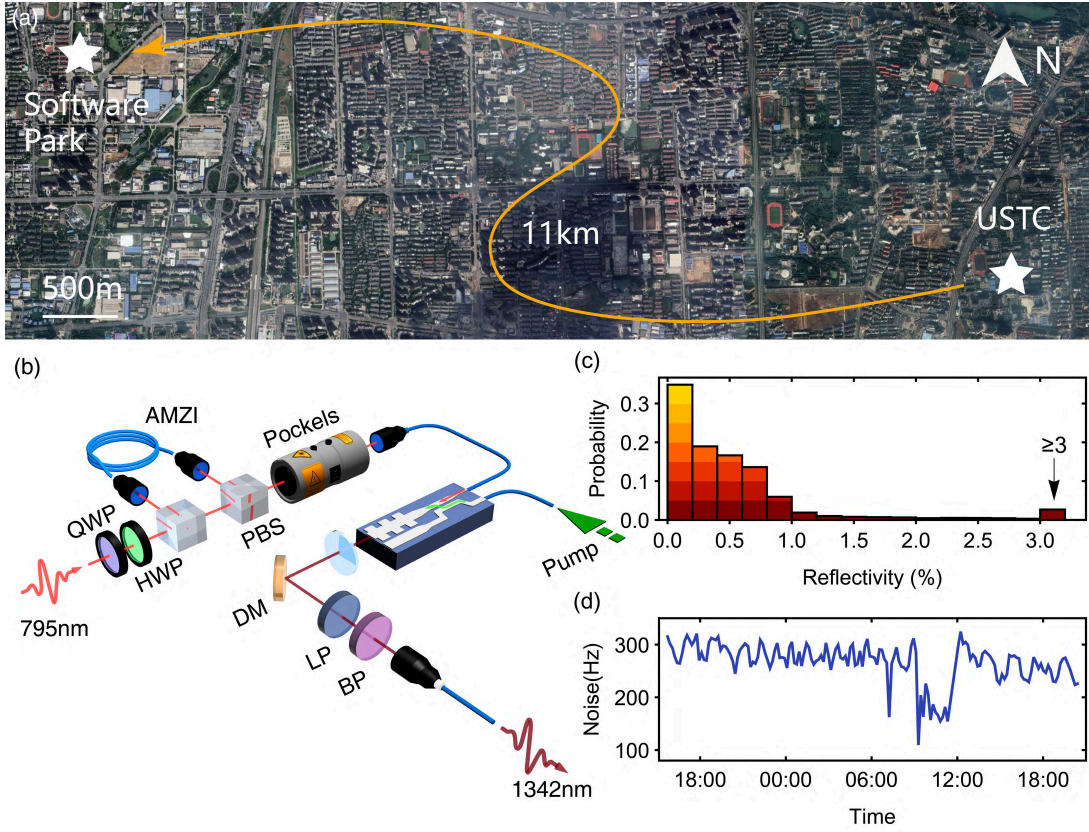


FIG. 4. **Entanglement over field fibers.** **a,** Bird's-eye view of remote entanglement experiment over the field fiber. Two quantum nodes are located in USTC. Telecom photons from two nodes are transmitted through two parallel field-deployed fibers to the middle station located at Software Park of Hefei. Each fiber is 11 km long and has an 4 dB attenuation for 1342 nm photon. **b,** Setup for polarization photon QFC. Two PBSs and a coiled polarization maintaining (PM) delay fiber constitute an AMZI. Two orthogonal polarization components ( $|\odot\rangle / |\oslash\rangle$ ) of 795 nm photon are separated in time domain after the AMZI and actively erased the polarization information by a Pockels cell. Then the time-bin encoded photon is sent to the QFC module. **c,** Possibility distribution of the reflectivity in the polarization filter PBS with the polarization compensation on. The data shown was recorded once per second and accumulated 24 hours. **d,** Background noise in SNSPD during 24 hours. Map data: Google Earth.



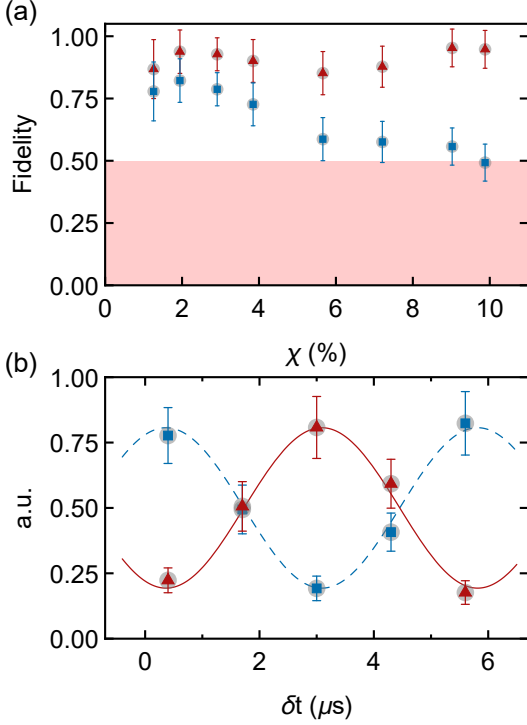


FIG. 5. **Characterization of the remote entanglement via TPI.** **a**, Fidelity of the remote entanglement generated locally as a function of  $\chi$ . Blue (square) dots refer to the measurement result. Red (triangle) dots shows the corrected results through deduction of accidental coincidences (see Supplementary Information). **b**, Two identical magnetic field applied in Node-A and B make sure  $|\Psi_{AB}^{\pm}\rangle$  invariant along with time evolution. To observe the coherence between its two components, we measure two spin-waves in  $|\uparrow\rangle \pm |\downarrow\rangle$  basis nearly simultaneously but with a little delay  $\delta t$  in Node-A. Depicted shows the oscillation of the parallel correlation (blue, square) and the cross correlation (red, triangle) as a function of  $\delta t$ . Sinusoids with corresponding colors (shaded and solid in shape) show the fitting result. The  $5.4 \mu s$  oscillation period is agreed with Zeeman splitting.

can be estimated as  $\mathcal{F} = \frac{1}{4}(1 + V_1 + 2V_2) = 0.714 \pm 0.028$ , which is proximate to the case of short fiber without QFC ( $\mathcal{F} = 0.739 \pm 0.082$ ).

### Entanglement over 50 km coiled fibers

Next we perform a two-node experiment via single-photon interference (SPI) [7]. As shown in Fig. 1, two pairs of Fock-state entanglement are created at Node-A and B respectively in the form of  $|0_p 0_e\rangle + \sqrt{\chi}|1_p 1_e\rangle$ , where 0 and 1 represent the number of photons or excitations. Then the frequency converted photons from both nodes are transmitted along a long fiber, later combined through a fiber beamsplitter (BS) to perform SPI and eliminate its “which way” information, finally detected with SNSPDs. A click from  $D_a$  or  $D_b$  heralds that two

ensembles are mapped into a maximally entangled state

$$|\Psi_e^{\pm}\rangle_{AB} = |0_e 1_e\rangle \pm e^{i\Delta\phi_{wo}} |1_e 0_e\rangle, \quad (2)$$

where  $|1_e\rangle$  and  $|0_e\rangle$  refer to Fock states of atomic excitations inside an ensemble and  $\Delta\phi_{wo}$  is the accumulated phase difference between two fiber channels. To keep  $\Delta\phi_{wo}$  in Eq. 2 constant, we harness a intermittent phase-locking loop in situ during every experimental interval to eliminate phase drift (see Methods).

Given a heralding signal, to verify the entanglement between the two atomic ensembles, we map the collective excitations into read-out fields as

$$\begin{aligned} \rho_{AB}^{ro} = & c_{00} |00\rangle \langle 00| + c_{+} |\Psi_p^{+}\rangle \langle \Psi_p^{+}| + \\ & c_{-} |\Psi_p^{-}\rangle \langle \Psi_p^{-}| + c_{11} |11\rangle \langle 11| + A.D., \end{aligned} \quad (3)$$

where 0 (1) and  $|\Psi_p^{\pm}\rangle$  are photon number and Bell-state of the read-out mode. *A.D.* refers to anti-diagonal items. This effective maximally entangled (EME) state in DLCZ protocol could be efficiently purified to polarization maximally entangled (PME) state and the intrinsic vacuum part be eliminated [7]. Hence, we consider the post-selected fidelity  $\mathcal{F}_{ro,post} = \frac{1}{2}(V_F + V_{\theta})$  with at least one read-out photon being detected to avoid the disturbance of vacuum part here (see Methods). Visibility  $V_F \equiv (c_{+} + c_{-}) / (c_{+} + c_{-} + c_{11})$  could be given directly by detecting two read-out modes and counting the corresponding events since it is not phase sensitive. To quantify  $V_{\theta} \equiv (c_{+} - c_{-}) / (c_{+} + c_{-} + c_{11})$ , we add a relative phase  $\theta$  between two read-out modes and mix them via a BS (see Supplementary Information and ref [16]). Along with the scan of  $\theta$ , counts in two output modes vary as a sinusoidal function of  $\theta$  as shown in Fig. 6, thus  $V_{\theta}$  could be deduced. In the DLCZ protocol, the choice of  $\chi$  affects the relative contributions of dark counts, single-excitation events and higher-order events. Via optimization without QFC (short fiber  $L=10$  m), We find a maximal fidelity of  $\mathcal{F}_{ro,post} = 0.896 \pm 0.018$  when  $\chi = 0.015$ . In this condition, the entangling probability in one trial is  $P_{ent} = 0.0132$  (see Methods), which is the highest probability of heralded remote entanglement creation, to the best of our knowledge.

In the long fiber ( $L=10$  km and 50 km) cases, we add the QFC module. The phase noise during long fiber transmission fluctuates faster [39] than the capable band of intermittent phase-locking. Hence we additionally insert an auxiliary continuous 1550 nm laser beam to uninterruptedly monitor phase fluctuation and actively stabilize it (see Methods). Measured results for the read-out photon interference at different fiber lengths are shown in Fig. 6. By fitting the sinusoidal oscillations, we get a fidelity result of  $\mathcal{F}_{ro,post} = 0.842 \pm 0.013$  for 10 km fiber and  $\mathcal{F}_{ro,post} = 0.832 \pm 0.019$  for 50 km fiber. Degradation of fidelity in comparison to the case of short fiber without QFC is mainly due to the remaining phase noise after stabilization (see methods), which can be improved significantly by optimizing the feedback loop. The heralded entangling probability is  $P_{ent} = 1.76 \times 10^{-3}$  for 10 km

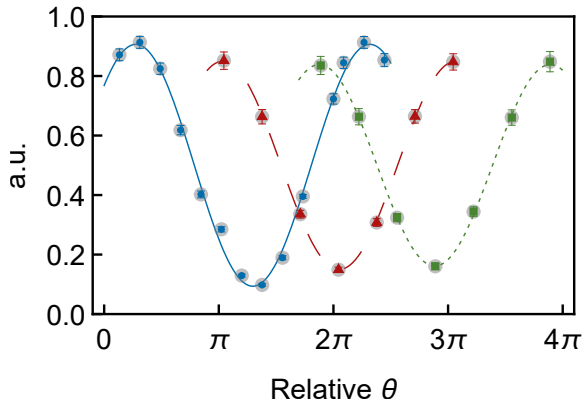


FIG. 6. **Characterization of the remote entanglement via SPI.** When creating distant entanglement via SPI, spin-wave mode is mapped onto read-out mode and be measured by  $\hat{\sigma}_\theta$ . Points shown is normalized ratio of parallel correlation as the function of  $\theta$ . Blue squares, red triangles and green dots refer to  $L=10$  m, 10 km and 50 km separately. Sinusoids with corresponding color (solid, dashed and dotted in shape) show the fitting results.

fiber and  $P_{ent} = 4.43 \times 10^{-4}$  for 50 km fiber, which correspond to an entanglement creation time of  $T_{ent} = 28$  ms and 0.56 s respectively (see Methods).

### Discussion and Outlook

We have experimental demonstrated two feasible ways to establish entanglement between two quantum memories via long-distance photon transmission in optical fibers. The TPI experiment merely requires photons being indistinguishable, thus is immune to phase fluctuations. Further extension of the TPI experiment to long-distance separated nodes is straightforward, which merely requires remote synchronization of control laser frequencies. While the SPI experiment has the benefit of higher entangling rate since it merely suffers from half of the channel loss. Further extension of the SPI experiment to long-distance separated nodes requires development of better phase stabilization of the fiber and remote phase synchronization of the control lasers (see Supplementary Information).

The remote entanglement generation time in our SPI experiment is already comparable with the best storage lifetime of atomic ensemble based quantum memories [31, 40]. There are several promising way of further increasing the entanglement generation rate. One may use Rydberg blockade to inhibit the high-order excitations during atom-photon entanglement preparation, and make the preparation process deterministic [41–43]. One may also make use of the multiplexing technique [44, 45] to prepare multiplexed atom-photon entanglement [46]. Shifting the wavelength to telecom C band, optimizing the coupling efficiencies and using better detectors will also increase the remote entanglement rate significantly.

Extending current experiments to remote separate quantum nodes, will enable to perform advanced quantum information tasks over it, such as efficient quantum teleportation over long distance. Incorporating more quantum memories, our experiment may be extended to entangle multiple quantum memories over long distances via multi-photon interference [30]. One may also create two pairs of remote atomic entanglement over two sub-links and extend the distance of atomic entanglement via entanglement swapping, following the scheme of quantum repeater [28]. Concatenating this process will extend the distance to the regime that beats direct transmission [6].

### Methods

**Time sequences.** The repetition rate of our experiment is  $\sim 50$  Hz. Within each cycle, the starting 18 ms is used for the MOT loading and active phase-locking. Afterwards, about 400 trials of experiment are performed before next MOT loading. Each trial last 5  $\mu$ s including 3  $\mu$ s for optical pumping and 2  $\mu$ s for write and read process.

**AMZI in the TPI experiment and its stabilization.** In TPI experiment, we apply two AMZIs to the write-out photon in each node. Each AMZI is constituted by two PBSs and a 30 m polarization maintaining (PM) delay fiber as shown in Fig. 4b. The short arm is in free space and the long arm is aligned with the slow-axis of the PM fiber. The 150 ns optical path difference between two arms is slightly larger than the write-out photon pulse width. To stabilize the AMZI, a 795 nm probe beam (linewidth  $\sim 1$  MHz) was introduced and picked up before and after it by two acoustic-optical-modulators (AOMs). Stabilization process only works in MOT loading phase. Test result shows a  $11.7^\circ$  phase uncertainty of it (see Supplementary Information).

**Active polarization compensation of the field fiber.** In the experiment over the field fiber, we replace the PCs in Fig. 1 by electric polarization controllers (EPCs). Adjusting the EPC to suppress the reflective signal in filtering PBS, we can dynamically compensate the polarization walk-off.

**Concatenated phase locking in the SPI experiment.** During the SPI experiment, write-“write-out” in entanglement building and read-“read-out” in measurement process form two interferometers, which need to be actively stabilized. However, we set a small angle between write (read) pulse and write-out (read-out) photon to suppress background noise. Therefore, probe beam cannot mimic phase evolution consistently. We rearrange the configuration as write-read and “write-out”-“read-out” two new interferometers (proof of consistence in Supplementary Information). In these two new interferometers, we first introduce an intermittent 795nm phase-locking beam separately and perform active feedback during every 18 ms MOT loading process to keep phase constantly. Propagation phase of pump laser is also involved because locking beam is converted by QFC module. In long distance situation, phase differ-

ence in fiber channels quivers faster than locking band. So we additionally introduce another auxiliary continuous 1550 nm beam and corresponding feedback circuit to assist suppressing high frequency noise uninterruptedly. This beam is leaded in and out via coarse wavelength division multiplexers (CWDMs) onto the long fiber.

**Post-selected fidelity in the SPI experiment.** In the subspace we concern, there exists a complete set of normal orthogonal bases,  $\{|00\rangle_{AB}, |11\rangle_{AB}, |\Psi^+\rangle_{AB}, |\Psi^-\rangle_{AB}\}$ . Supposing the maximally entangled state  $|\Psi^+\rangle_{AB}$  we want, when post-select at least one photon be detected, we get  $\mathcal{F}_{ro,post} = \langle \Psi^+ | \rho | \Psi^+ \rangle = c_+ / (c_+ + c_- + c_{11})$ .  $c_{00}$ ,  $c_{11}$  and sum of  $c_+$  and  $c_-$  can be directly known by measurement shown in Fig. 1. Here we define Fock visibility  $V_F = (c_1^+ + c_1^-) / (c_1 + c_2)$ . To tell  $c_+$  and  $c_-$  separately, we combine two read-out optical mode together via a BS. A clicking event from one of two outputs corresponds to a projecting measurement of  $\hat{\sigma}_\theta = |01\rangle_{AB}\langle 01| \pm e^{i(\theta + \Delta\phi_{ro})} |10\rangle_{AB}\langle 10|$ . Guaranteed  $\phi_{ro}$  fixed, when  $\theta = 0$  or  $\pi$ , count ratio in one output corresponds to  $c_+$  ( $c_-$ ). Double excitation coincidence in probability  $c_{11}$  will contribute to two counts equally. Therefore,  $V_\theta = (c_+ - c_-) / (c_+ + c_- + c_{11})$ . Post-selected fidelity then could be written as  $\mathcal{F}_{ro,post} = (V_F + V_\theta) / 2$ .

**Limitation of fidelity in the SPI experiment.** Homogeneity of two write-out (read-out) photons from different ensembles determines the quality of interference. So we check them via Hong-Ou-Mandel (HOM) experiment and find HOM visibility  $V_{wo} = 0.082$  and  $V_{ro} = 0.074$  respectively, which gives main limit to  $V_\theta$  (see Supplementary information). Besides, we analyze three possible origins of fidelity decreasing in long distance situation. First one is the phase instability. By means of active and assistant phase stabilization, we do our best to restrain phase fluctuation. But there are

still  $8.3^\circ$  and  $13.4^\circ$  standard deviation for 10 km and 50 km situation respectively. Second one is the decline of SNR. Noise from frequency conversion will not affect SNR through transmission due to similar loss for signal and QFC noise. However, phase stabilization process brings new noises and the contribution of dark counts of SNSPD grows up along with the attenuation of signal. Finally, we get SNR as 10 : 1 and 5 : 1 respectively. Third one is the mismatch between two optical paths. We precisely check the arriving time of write-out photon by fitting its profile. Results shows that about 2.10 ns and 1.45 ns time difference in 10 km and 50 km situation. Analysis shows these three imperfection bring  $0.011$ ,  $6 \times 10^{-3}$ ,  $5.8 \times 10^{-3}$  and  $0.027$ ,  $0.020$ ,  $3 \times 10^{-3}$  infidelity to  $\mathcal{F}_{ro,post}$  in 10 km and 50 km situation separately (see Supplementary Information).

**Remote entanglement generation time.** In SPI experiments, the probability of remote entanglement creation is  $P_{ent} = 2\chi\eta_{QFC}\eta_{loss}\sqrt{\eta_{fiber}\eta_{det}}$ , where  $\eta_{loss}$ ,  $\eta_{fiber}$  and  $\eta_{det}$  are efficiencies of photon coupling, fiber transmission and detector, respectively. In the whole experiment, we calibrate  $\chi$  by detecting 795 nm write-out photon locally and deducing  $\eta_{loss}$  and the detection efficiency of silicon avalanche photon-diode. In QFC-free and short fiber case, we have  $P_{ent} = 1.32 \times 10^{-2}$ . In the long fiber cases, we have  $P_{ent} = 1.76 \times 10^{-3}$  and  $4.43 \times 10^{-4}$  for 10 km and 50 km setting. Considering the telecommunication time  $T_{com}$  for a distance, we can estimate the average time for entanglement creation as  $T_{ent} = \frac{1}{P_{ent}}T_{com}$ . For 10 km situation, we get  $T_{ent}$  equals to 28 ms, which is far lower than 0.22 s spin-wave lifetime achieved by Yang et al.[40] in  $^{87}\text{Rb}$  atomic ensemble. For 50 km situation with 250  $\mu\text{s}$ , we need 0.56 s to build an entanglement, also comparable to 0.22 s spin-wave lifetime.

- 
- [1] Kimble, H. J. The quantum internet. *Nature* **453**, 1023–1030 (2008).
  - [2] Yuan, Z.-S. *et al.* Entangled photons and quantum communication. *Physics Reports* **497**, 1–40 (2010).
  - [3] Wehner, S., Elkouss, D. & Hanson, R. Quantum internet: A vision for the road ahead. *Science* **362**, eaam9288 (2018).
  - [4] Inagaki, T., Matsuda, N., Tadanaga, O., Asobe, M. & Takesue, H. Entanglement distribution over 300 km of fiber. *Optics Express* **21**, 23241 (2013).
  - [5] Yin, J. *et al.* Satellite-based entanglement distribution over 1200 kilometers. *Science* **356**, 1140–1144 (2017).
  - [6] Sangouard, N., Simon, C., de Riedmatten, H. & Gisin, N. Quantum repeaters based on atomic ensembles and linear optics. *Reviews of Modern Physics* **83**, 33–80 (2011).
  - [7] Duan, L.-M., Lukin, M. D., Cirac, J. I. & Zoller, P. Long-distance quantum communication with atomic ensembles and linear optics. *Nature* **414**, 413–418 (2001).
  - [8] Simon, C. & Irvine, W. T. M. Robust Long-Distance Entanglement and a Loophole-Free Bell Test with Ions and Photons. *Physical Review Letters* **91**, 110405 (2003).
  - [9] Gottesman, D., Jennewein, T. & Croke, S. Longer-Baseline Telescopes Using Quantum Repeaters. *Physical Review Letters* **109**, 070503 (2012).
  - [10] Kómár, P. *et al.* A quantum network of clocks. *Nature Physics* **10**, 582–587 (2014).
  - [11] Tittel, W. *et al.* Photon-echo quantum memory in solid state systems. *Laser & Photonics Reviews* **4**, 244–267 (2009).
  - [12] Duan, L.-M. & Monroe, C. Colloquium : Quantum networks with trapped ions. *Reviews of Modern Physics* **82**, 1209–1224 (2010).
  - [13] Reiserer, A. & Rempe, G. Cavity-based quantum networks with single atoms and optical photons. *Reviews of Modern Physics* **87**, 1379–1418 (2015).
  - [14] Aharonovich, I., Englund, D. & Toth, M. Solid-state single-photon emitters. *Nature Photonics* **10**, 631–641 (2016).
  - [15] Julsgaard, B., Kozhekin, A. & Polzik, E. S. Experimental long-lived entanglement of two macroscopic objects.

- Nature* **413**, 400–836 (2001).
- [16] Chou, C. W. *et al.* Measurement-induced entanglement for excitation stored in remote atomic ensembles. *Nature* **438**, 828–832 (2005).
  - [17] Chou, C.-W. *et al.* Functional Quantum Nodes for Entanglement Distribution over Scalable Quantum Networks. *Science* **316**, 1316–1320 (2007).
  - [18] Yuan, Z.-S. *et al.* Experimental demonstration of a BDCZ quantum repeater node. *Nature* **454**, 1098–1101 (2008).
  - [19] Hofmann, J. *et al.* Heralded Entanglement Between Widely Separated Atoms. *Science* **337**, 72–75 (2012).
  - [20] Bernien, H. *et al.* Heralded entanglement between solid-state qubits separated by three metres. *Nature* **497**, 86–90 (2013).
  - [21] Hensen, B. *et al.* Loophole-free Bell inequality violation using electron spins separated by 1.3 kilometres. *Nature* **526**, 682–686 (2015).
  - [22] Humphreys, P. C. *et al.* Deterministic delivery of remote entanglement on a quantum network. *Nature* **558**, 268–273 (2018).
  - [23] Delteil, A. *et al.* Generation of heralded entanglement between distant hole spins. *Nature Physics* **12**, 218–223 (2015).
  - [24] Moehring, D. L. *et al.* Entanglement of single-atom quantum bits at a distance. *Nature* **449**, 68–71 (2007).
  - [25] Slodička, L. *et al.* Atom-Atom Entanglement by Single-Photon Detection. *Physical Review Letters* **110**, 83603 (2013).
  - [26] Kumar, P. Quantum frequency conversion. *Optics Letters* **15**, 1476 (1990).
  - [27] Zhao, B., Chen, Z.-B., Chen, Y.-A., Schmiedmayer, J. & Pan, J.-W. Robust Creation of Entanglement between Remote Memory Qubits. *Physical Review Letters* **98**, 240502 (2007).
  - [28] Briegel, H.-J., Dür, W., Cirac, J. I. & Zoller, P. Quantum Repeaters: The Role of Imperfect Local Operations in Quantum Communication. *Physical Review Letters* **81**, 5932–5935 (1998).
  - [29] Yang, S.-j. *et al.* Highly Retrievable Spin-Wave Photon Entanglement Source. *Physical Review Letters* **114**, 210501 (2015).
  - [30] Jing, B. *et al.* Entanglement of three quantum memories via interference of three single photons. *Nature Photonics* **13**, 210–213 (2019).
  - [31] Radnaev, A. G. *et al.* A quantum memory with telecom-wavelength conversion. *Nature Physics* **6**, 894–899 (2010).
  - [32] De Greve, K. *et al.* Quantum-dot spin-photon entanglement via frequency downconversion to telecom wavelength. *Nature* **491**, 421–425 (2012).
  - [33] Maring, N. *et al.* Photonic quantum state transfer between a cold atomic gas and a crystal. *Nature* **551**, 485 (2017).
  - [34] Bock, M. *et al.* High-fidelity entanglement between a trapped ion and a telecom photon via quantum frequency conversion. *Nature Communications* **9**, 1998 (2018).
  - [35] Ikuta, R. *et al.* Polarization insensitive frequency conversion for an atom-photon entanglement distribution via a telecom network. *Nature Communications* **9**, 1997 (2018).
  - [36] Walker, T. *et al.* Long-Distance Single Photon Transmission from a Trapped Ion via Quantum Frequency Conversion. *Physical Review Letters* **120**, 203601 (2018).
  - [37] Dréau, A., Tchekhovateva, A., Mahdaoui, A. E., Bonato, C. & Hanson, R. Quantum Frequency Conversion of Single Photons from a Nitrogen-Vacancy Center in Diamond to Telecommunication Wavelengths. *Physical Review Applied* **9**, 064031 (2018).
  - [38] Jiang, Y., Rui, J., Bao, X.-H. & Pan, J.-W. Dynamical zeroing of spin-wave momentum to suppress motional dephasing in an atomic-ensemble quantum memory. *Physical Review A* **93**, 063819 (2016).
  - [39] Minář, J., De Riedmatten, H., Simon, C., Zbinden, H. & Gisin, N. Phase-noise measurements in long-fiber interferometers for quantum-repeater applications. *Physical Review A* **77**, 052325 (2008).
  - [40] Yang, S.-J., Wang, X.-J., Bao, X.-H. & Pan, J.-W. An efficient quantum light-matter interface with sub-second lifetime. *Nature Photonics* **10**, 381 (2016).
  - [41] Saffman, M., Walker, T. G. & Mølmer, K. Quantum information with Rydberg atoms. *Reviews of Modern Physics* **82**, 2313–2363 (2010).
  - [42] Li, L., Dudin, Y. O. & Kuzmich, A. Entanglement between light and an optical atomic excitation. *Nature* **498**, 466–469 (2013).
  - [43] Li, J. *et al.* Hong-ou-mandel interference between two deterministic collective excitations in an atomic ensemble. *Physical review letters* **117**, 180501 (2016).
  - [44] Pu, Y.-F. *et al.* Experimental realization of a multiplexed quantum memory with 225 individually accessible memory cells. *Nature Communications* **8**, 15359 (2017).
  - [45] Tian, L. *et al.* Spatial Multiplexing of Atom-Photon Entanglement Sources using Feedforward Control and Switching Networks. *Physical Review Letters* **119**, 130505 (2017).
  - [46] Collins, O. A., Jenkins, S. D., Kuzmich, A. & Kennedy, T. A. B. Multiplexed Memory-Insensitive Quantum Repeaters. *Physical Review Letters* **98**, 060502 (2007).

### Acknowledgment

This work was supported by National Key R&D Program of China (No. 2017YFA0303902), Anhui Initiative in Quantum Information Technologies, National Natural Science Foundation of China, and the Chinese Academy of Sciences. We acknowledge QuantumCTek for providing the field-deployed fibers.



## SUPPLEMENTARY INFORMATION

### I. DETAILS OF AMZI STABILIZATION IN TPI EXPERIMENT

In TPI experiment, we actively stabilize the AMZI in each node. Here we give the locking scheme and its text result. Fitting results show that the deviation for is  $5.88^\circ$  probe beam, and  $11.68^\circ$  for signal.

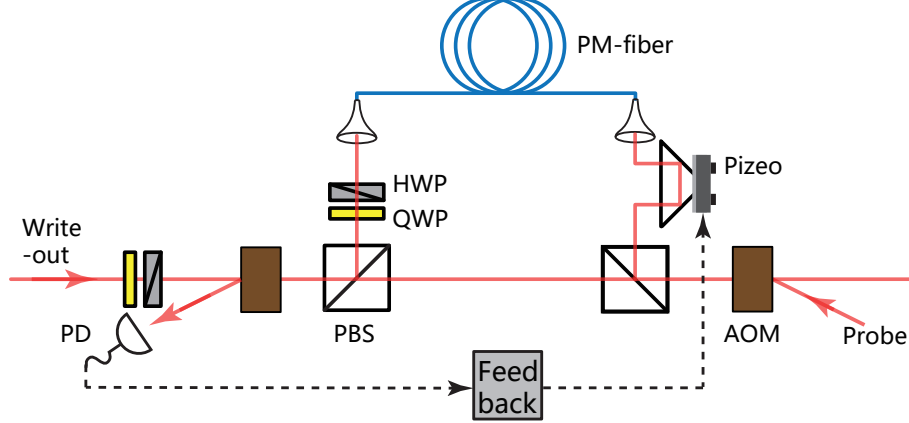


FIG. S1. Configuration of AMZI stabilization.

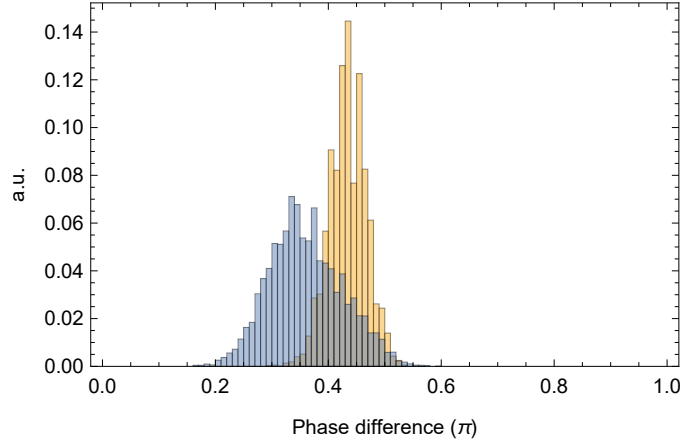


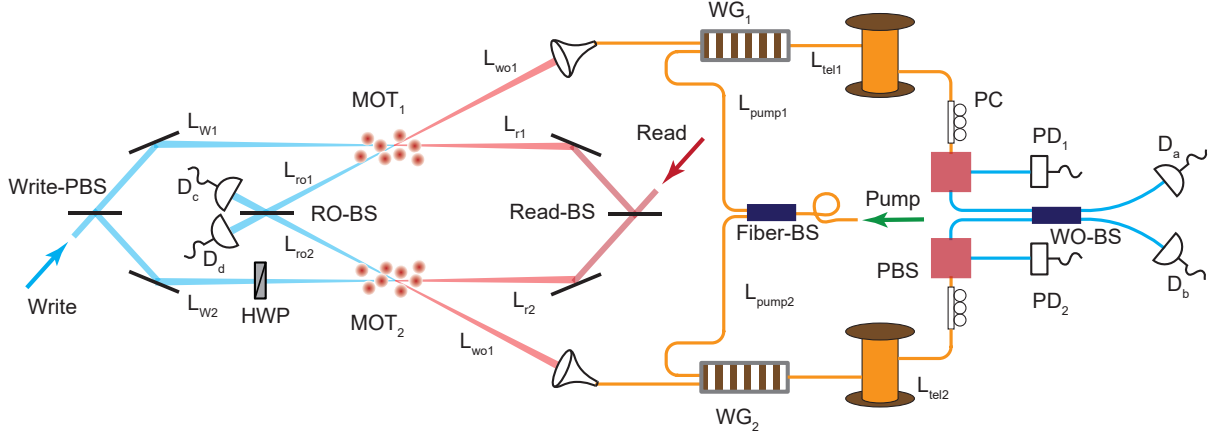
FIG. S2. Results of AMZI stabilization. Yellow for probe beam and blue for signal.

### II. DETAILS OF PHASE-STABILIZATION IN SPI EXPERIMENT

#### A. Measurement configuration

When performing measurement  $\hat{\sigma}_\theta$ , one of difficulties is to assure phase stabilized between write beams in write process, read beams in retrieval process, pump lasers in QFC process, write-out fields along long fiber channel and read-out fields in measurement. Here we prove that all these problems can be solved by stabilizing two interferometers.

As depicted in Fig. S3, we label the distance from Write-BS to MOT<sub>1</sub> (MOT<sub>2</sub>) as  $L_w^1$  ( $L_w^2$ ), distance from Read-BS to MOT<sub>1</sub> (MOT<sub>2</sub>) as  $L_r^1$  ( $L_r^2$ ) and distance from MOT<sub>1</sub> (MOT<sub>2</sub>) to RO-BS as  $L_{ro}^1$  ( $L_{ro}^2$ ). Similarly, we denote the distance from MOT<sub>1</sub> (MOT<sub>2</sub>) to the front facet of WG<sub>1</sub> (WG<sub>2</sub>) as  $L_{wo}^1$  ( $L_{wo}^2$ ), the distance from Fiber-BS to the front facet of WG<sub>1</sub> (WG<sub>2</sub>) as  $L_{pump}^1$  ( $L_{pump}^2$ ), and the distance from the end facet of WG<sub>1</sub> (WG<sub>2</sub>) to WO-BS as  $L_{tel}^1$

FIG. S3. Detailed configuration of  $V_\theta$  measurement.

( $L_{tel}^2$ ). Still, in case the imperfection of manufacturing, we assume the length of a PPLN waveguide chip separately as  $L_{WG}^1$  and  $L_{WG}^1$ .

First, we take the Write-BS and WO-BS as two beam-splitters of Mach-Zehnder interferometer, and two Write-write-out-QFC process as two arms of interferometer. The phase accumulation of two arms could be written as:

$$\phi_{wi} = \frac{L_w^i}{\lambda_w} - \phi_{MOT}^i + \frac{L_{wo}^i}{\lambda_{wo}} + \frac{L_{WG}^i + L_{tel}^i}{\lambda_{tel}} - \frac{L_{pump}^i}{\lambda_{pump}}, \quad i = 1, 2 \quad (S1)$$

$\phi_{MOT}^i$  represent the phase adding up to atom ensemble during spontaneous Raman scattering. Here we assume there are no uncertainty in the frequency conversion process, i.e. the conversion process always happen in the front facet of the PPLN waveguide chip. We will show that this assumption is reasonable later in the Sec. II B.

Similarly, we could write the phase accumulation in read-read-out process:

$$\phi_r^i = \frac{L_r^i}{\lambda_r} + \phi_{MOT}^{i'} + \frac{L_{ro}^i}{\lambda_{ro}}, \quad i = 1, 2. \quad (S2)$$

The difference between  $\phi_{MOT}^i$  and  $\phi_{MOT}^{i'}$  comes from phase evolution of a certain energy level of atom. Due to the internal time between write and read process is fixed, it is obvious that

$$\phi_{MOT}^{i'} - \phi_{MOT}^i = \text{constant}. \quad (S3)$$

In phase stabilization condition, we have

$$\phi_w^1 = \phi_w^2 + n\pi, \quad \phi_r^1 = \phi_r^2 + m\pi. \quad (S4)$$

$n$  and  $m$  are two integers. Combing Eq. S1 to Eq. S4, we can easily conclude two equations as follow,

$$\frac{L_w^1}{\lambda_w} + \frac{L_r^1}{\lambda_r} = \frac{L_w^2}{\lambda_w} + \frac{L_r^2}{\lambda_r} + n'\pi \quad (S5)$$

$$\begin{aligned} \frac{L_{ro}^1}{\lambda_{ro}} + \frac{L_{wo}^1}{\lambda_{wo}} + \frac{L_{WG}^1 + L_{tel}^1}{\lambda_{tel}} - \frac{L_{pump}^1}{\lambda_{pump}} \\ = \frac{L_{ro}^2}{\lambda_{ro}} + \frac{L_{wo}^2}{\lambda_{wo}} + \frac{L_{WG}^2 + L_{tel}^2}{\lambda_{tel}} - \frac{L_{WG}^2}{\lambda_{pump}} + m'\pi \end{aligned} \quad (S6)$$

Eq. S5 and Eq. S6 refers to two Mach-Zehnder interferometer as depicted as Fig. S4. The first one takes Write-PBS and Read-BS as two beamsplitters of interferometer and covers paths of write and read beams. Therefore we introduce a 795 nm locking beam from the idle port of Read-BS to detect the interference signal in the second output of the Write-BS and feed it back to delay. A combination of two half-wave-plate (HWPs) and a quarter-wave-plate (QWP) in

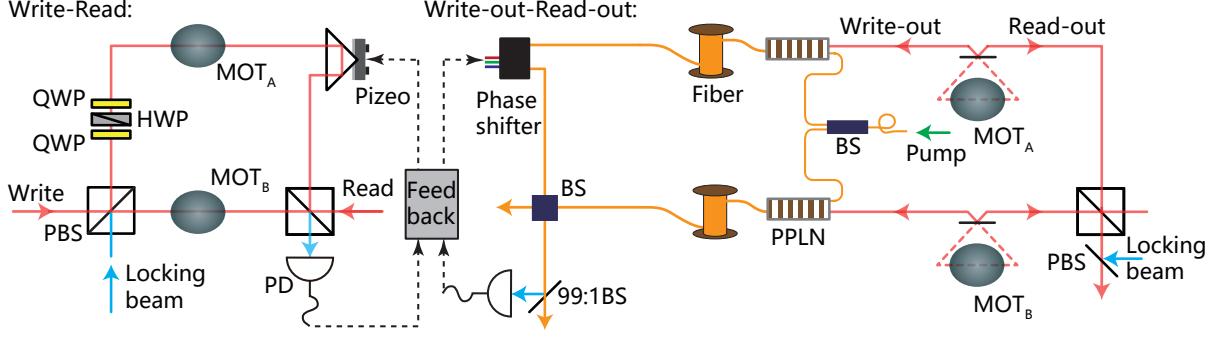


FIG. S4. Configuration of phase stabilization. Phase stabilization include two interferometer, i.e. write-read and write-out-read-out.

sandwich configuration introduce a relative phase  $\theta$  between phase-locking laser and the write beam without changing their polarization. The second one takes WO-BS and RO-BS as two beamsplitters of interferometer and covers paths of write-out and read-out photons, meanwhile including the frequency conversion module and several kilometer long fibers. We introduce another locking beam from RO-BS using a 1 : 99 BS and detect the interference signal in the WO-BS in the same way. The frequency of this beam is far detuning from the resonance point of cavity, hence no interaction with atoms. In this method, we assume the scale of MOT is 0. Actually, there still exist a little uncertainty of phase difference introduced by the non-zero scale of MOT. But we will prove it small enough in Sec. II B.

We detune the frequency of this laser far detuning from the resonance point of cavity. Hence this laser will not interact with atoms.

### B. Phase uncertainty in PPLN waveguide chips and atomic ensembles

In DFG process, we always have the energy conservation principal

$$\frac{1}{\lambda_{Signal}} = \frac{1}{\lambda_{Pump}} + \frac{1}{\lambda_{Telecom}}. \quad (S7)$$

Supposing DFG happens  $x$  from the front facet of the PPLN waveguide chip as depicted in Fig. S5a, then the phase accumulation of optical field is

$$\begin{aligned} \phi &= \frac{x}{\lambda_{Signal}} - \frac{x}{\lambda_{Pump}} + \frac{L-x}{\lambda_{Telecom}} \\ &= x \cdot \left( \frac{1}{\lambda_{Pump}} + \frac{1}{\lambda_{Telecom}} \right) - \frac{x}{\lambda_{Pump}} + \frac{L-x}{\lambda_{Telecom}} \\ &= \frac{L}{\lambda_{Telecom}}. \end{aligned} \quad (S8)$$

which means we can always assume DFG happening at the front facet of the PPLN waveguides chip.

In former discussion about interferometer such as Eq. S5 and Eq. S6, we assume the atomic ensemble as a point with no scale and was settled in a certain point. Then we can ignore the change of wavelength after this point and using one laser to stabilize phase. Now we consider a real ensemble with diameter  $D$  as depicted in Fig. S5b, which is around  $100 \mu\text{m}$  in our system. Two laser here are both around  $\lambda = 795 \text{ nm}$  with  $\delta = 6.8 \text{ GHz}$  difference. First we assume the location where spontaneous Raman scattering happens in left and right edge of ensemble. The phase difference is

$$\begin{aligned} \Delta\theta &= 2\pi \cdot (D/\lambda_1 - D/\lambda_2) \\ &= 2\pi D \cdot \frac{\delta}{c} \approx 0.014 = 0.81^\circ. \end{aligned} \quad (S9)$$

It is plausible to consider this location obeys uniform distribution in this regime, we can easily know standard deviation of phase difference  $S$  as

$$S = \sqrt{\frac{\Delta\theta^2}{12}} \approx 4 \times 10^{-3} = 0.24^\circ. \quad (S10)$$

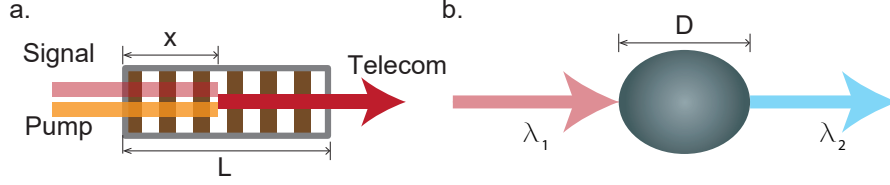


FIG. S5. a. Transition point uncertainty in a PPLN waveguides chip. b. Exciting position uncertainty in MOT.

So, theoretically, in perfect stabilizing condition, only  $0.24^\circ$  uncertainty of phase will be introduced.

### III. LASERS IN OUTDOOR APPLICATION

In current experiment, two atomic ensembles are placed nearly in one laboratory. For simplicity, two ensembles shared control beams (i.e. write, read and pump beams) from same lasers. Moreover, in phase stabilization process in SPI experiment, axillary beams to detect the phase difference between two paths are also split from one laser. In TPI experiments, lasers located in different node could be easily locked to an absolute frequency standard such as absorption spectrum or ultra stable cavity. But in SPI experiments, not only the frequency, but also the phase of lasers in different nodes need to be synchronized. There must be a question that is it necessary to share these control and auxiliary beams among distant nodes or actively lock their relative phase in outdoor application. Here we prove that all lasers in each node could works independently and give the request for each laser in different application situations.

#### A. Phase of control lasers

There are three main steps in DLCZ protocol, heralded entanglement creation in basic segments, a series of entanglement swapping and finally converting two EME states to a PME state. Without loss of generality, we observe three normal cases here to represent three steps respectively.

First, in entanglement creation step, we put only one laser in each node serving as write beam as depicted in Fig. S6a. In node-B, write beams for two ensembles are split from one laser. Suppose each laser has an initial phase  $\phi_A$ ,  $\phi_B$  and  $\phi_C$  respectively. Besides, we assume that all lasers work in the same frequency  $\omega_w$  and have very long coherent time. When one of  $D_a^1$  and  $D_a^2$  clicks and one of  $D_a^3$  and  $D_a^4$  clicks, the state of four ensembles become

$$|\Psi\rangle_{AB_L B_R C} = (e^{i\phi_A} |1_S 0_S\rangle_{AB_L} + e^{i\phi_B} e^{i\theta_{AB}} |0_S 1_S\rangle_{AB_L}) \otimes (e^{i\phi_B} |1_S 0_S\rangle_{B_R C} + e^{i\phi_C} e^{i\theta_{AB}} |0_S 1_S\rangle_{B_R C}) e^{i\omega_w \Delta t} e^{i\omega_p \Delta t}, \quad (\text{S11})$$

where  $\Delta t$  is time difference between entanglement  $MOT_A - MOT_B^L$  and  $MOT_B^R - MOT_C$  creation.  $\theta_{AB}$  and  $\theta_{BC}$  are stabilized phase in long fiber. Besides, the pump beam in QFC process brings an extra phase (initial phase of pump laser) between  $|0_S\rangle$  and  $|1_S\rangle$ , which is similar as the write beam. Therefore we consider the pump laser as a part of write laser and do not list it in the equation.

Next we perform entanglement swapping as in Fig. S6b. Spin-waves in  $MOT_B^L$  and  $MOT_B^R$  are mapped onto read-out optical fields with the help of read beams in frequency  $\omega_r$ . Since they are placed in one node, read beams are split from one laser with the initial phase  $\psi_B$ . After retrieval, the state of two ensembles and two optical fields become

$$|\Psi\rangle_{AB_L B_R C} = (e^{i\phi_A} |1_S 0_{ro}\rangle_{AB_L} + e^{i(\phi_B + \psi_B)} e^{i\theta_{AB}} |0_S 1_{ro}\rangle_{AB_L}) \otimes (e^{i(\phi_B + \psi_B)} |1_{ro} 0_S\rangle_{B_R C} + e^{i\phi_C} e^{i\theta_{BC}} |0_{ro} 1_S\rangle_{B_R C}) e^{i\omega_w \Delta t} e^{i\omega_p \Delta t}. \quad (\text{S12})$$

After two read-out fields interfere at middle BS, entanglement is swapped to  $MOT_A$  and  $MOT_C$  as

$$|\Psi\rangle_{AC} = (e^{i\phi_A} |1_S 0_S\rangle_{AC} + e^{i\phi_C} e^{i(\theta_{AB} - \theta_{BC})} |0_S 1_S\rangle_{AC}) e^{i\omega_w \Delta t} e^{i\omega_p \Delta t}. \quad (\text{S13})$$

Generally, during each quantum swapping process, the initial phase from middle laser is eliminated and the phase of final state only comes from long fiber and laser in end nodes.

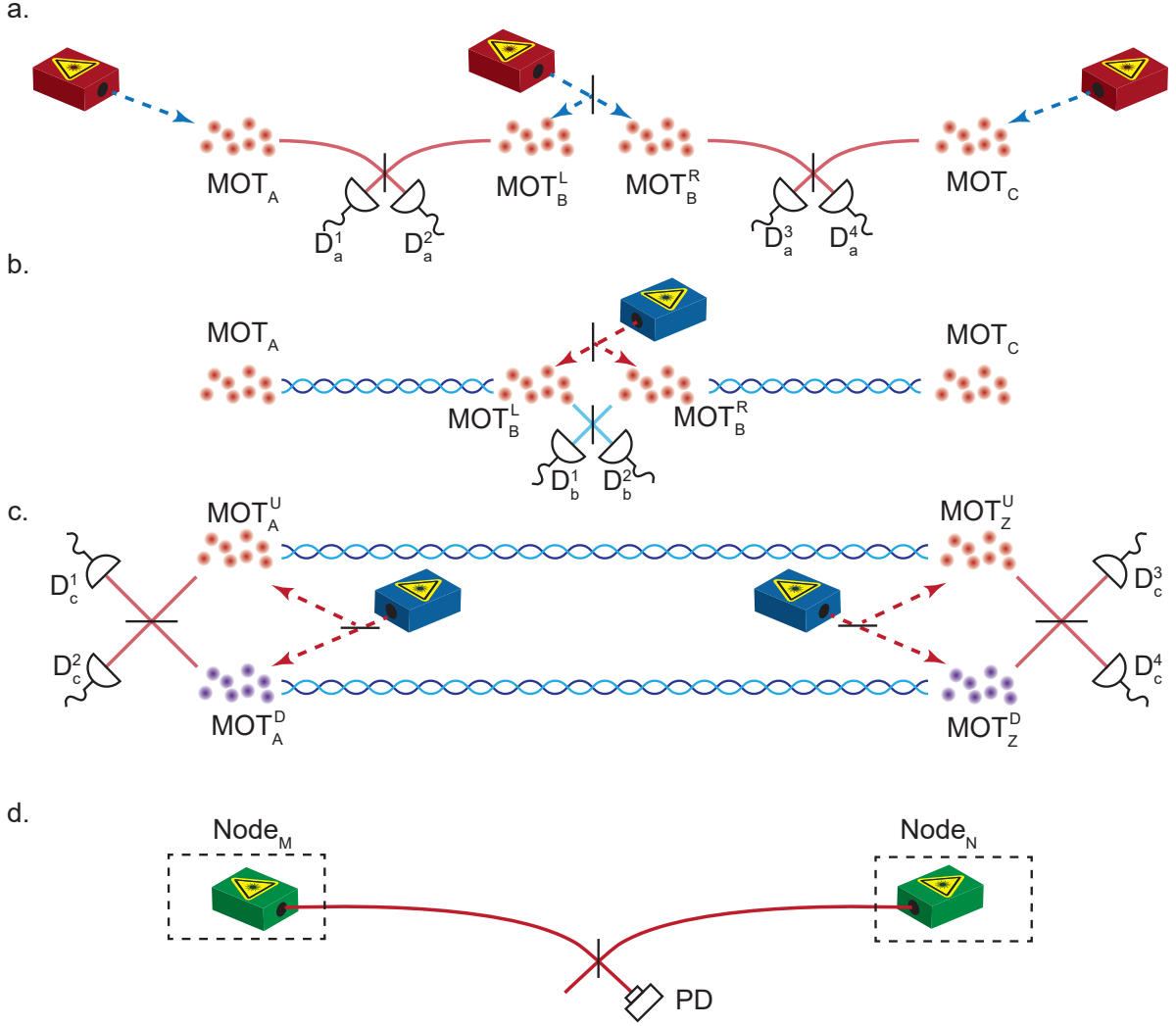


FIG. S6. Three main steps in DLCZ protocol. a. Herald entanglement creation in basic segments. b. Entanglement swapping. c. Converting two EME states to a PME state.

Finally, through entanglement creation in basic segments and a series of swapping, we get a pair of entanglement  $MOT_A^U - MOT_Z^U$  and  $MOT_A^D - MOT_Z^D$ . We convert these two EME states to a PME state. Mapping all spin-waves onto read-out fields we get

$$|\Psi\rangle_{A_U Z_U A_D Z_D} = (e^{i(\phi_A + \psi_A)} |1_{ro} 0_{ro}\rangle_{A_U Z_U} + e^{i(\phi_Z + \psi_Z)} e^{i\theta_{AZ}} |0_{ro} 1_{ro}\rangle_{A_U Z_U}) \otimes (e^{i(\phi_A + \psi_A)} |1_{ro} 0_{ro}\rangle_{A_D Z_D} + e^{i(\phi_Z + \psi_Z)} e^{i\theta_{AZ}} |0_{ro} 1_{ro}\rangle_{A_D Z_D}) e^{i\omega_w \Delta t} e^{i\omega_p \Delta t} e^{i\omega_r \Delta t'}, \quad (S14)$$

where  $\phi_A$  ( $\psi_A$ ) and  $\phi_Z$  ( $\psi_Z$ ) refer to initial phase of write (read) laser in node-A and Z.  $\Delta t'$  is the time difference between entanglement  $MOT_A^U - MOT_Z^U$  and  $MOT_A^D - MOT_Z^D$  generation. When we register only the coincidences of two-side detectors, the effective part contribute to final result is

$$|\Psi\rangle_{AZ} = (|1_{ro} 0_{ro}\rangle_{AZ} + |0_{ro} 1_{ro}\rangle_{AZ}) e^{i\omega_w \Delta t} e^{i\omega_p \Delta t} e^{i\omega_r \Delta t'}. \quad (S15)$$

We can see that the initial phase from all lasers, whatever nodes they are placed, are eliminated finally. Note that this conclusion is based on an assumption that a sufficient long coherent time for all lasers. How long exactly does the coherent time meet our needs? It is obvious that the coherent time of write lasers should be longer than  $\Delta t$  and



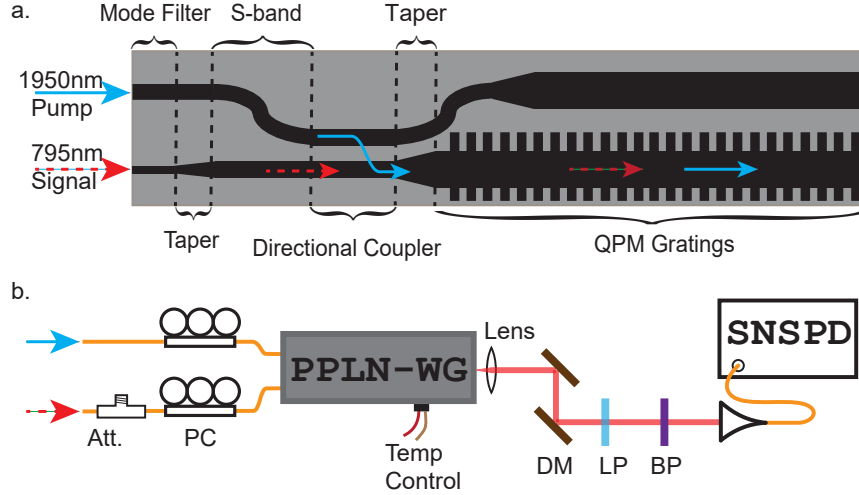


FIG. S7. a. Detailed structure inside a PPLN waveguide chip. b. Setup for test of a PPLN waveguides chip.

the coherent time of read lasers should be longer than  $\Delta t'$  so that their evolution phase can be expressed as a global phase in Eq. S15. These means *linewidth*  $< 1/\Delta t$  for write and pump lasers and *linewidth*  $< 1/\Delta t'$  for read lasers.

### B. Phase locking scheme

In outdoor application, two interference paths in one repeater segment still need to be stabilized. But here we try to probe the propagation phases of two paths by different lasers. As depicted in Fig. S6d, we put one laser in each node of a basic segment serving for phase locking. Suppose that they all work in the same frequency  $\omega_{ph}$  and have sufficient narrow linewidth. Two lasers beams transmit along the fiber channel and are combined in the middle BS. We could sift out these beams after the BS and detect their interference signal by a photodiode. The intensity on the photodiode is

$$I = I_A + I_B + 2\sqrt{I_A I_B} \cos \delta$$

$$\delta = (\theta_A - \theta_B) + (\theta_{AM}(t) - \theta_{MB}(t))$$
(S16)

where  $I_A$  and  $I_B$  is the beam intensity send from node-A and B. The fiber attenuation is neglect due to classical regime we are considering. We can see that when the coherent time of laser is sufficient long, the only factor influence interference result is the phase fluctuation in fiber channels. Thus it could be actively eliminated immediately. Similar as the analysis before, the coherent time of this laser should be longer than one trial time for DLCZ repeater protocol.

## IV. PPLN WAVEGUIDE CHIPS FABRICATION AND TEST

We fabricate reverse-proton-exchange (RPE) periodically-poled lithium niobate (PPLN) waveguide chips [1, 2] with a total length of 52 mm for difference-frequency generation (DFG) of 795 nm signal and 1950 nm pump. To couple the two very different wavelengths into the fundamental spatial mode of the same waveguide, we use an integrated waveguide structure consisting of a bent waveguide and a straight waveguide with an entrance center-to-center separation of 126  $\mu\text{m}$ , as shown in Fig. S7a.

The main features of the integrated structure are two individual mode filters optimizing the fiber-to-waveguide coupling efficiency of signal and pump respectively, a directional coupler [3] working as a wavelength combiner, and a uniform straight waveguide with 45-mm-long QPM gratings for optical frequency nonlinear mixing. The QPM period is 17.1  $\mu\text{m}$ .

A HI780 fiber for 795 nm signal and a SM-28e fiber for 1950 nm pump are terminated in a silicon V-groove array and pigtailed to the input of the waveguides. The 795 nm signal is coupled into the 2- $\mu\text{m}$ -wide mode filter and the 1950 nm pump is coupled into the 5- $\mu\text{m}$ -wide mode filter, with estimated fiber-to-waveguide coupling efficiencies of 89% and 74% respectively. The 1950 nm pump then goes through an adiabatic taper, a S-bend, and enters the

directional coupler. With a waveguide width of 5.5  $\mu\text{m}$ , an edge-to-edge spacing of 3.5  $\mu\text{m}$ , and a length of 0.3 mm, the directional coupler combines the 1950 nm pump and the 795 nm signal into the same straight waveguide with low losses simultaneously. We define the pump coupling efficiency as the ratio between the output power of the straight waveguide and the total output power, and define the signal coupling loss as the ratio between the output power of the bent waveguide and the total output power. The measured pump coupling efficiency is -0.3 dB and the signal coupling loss is negligible. The combined waves then enter the nonlinear mixing region with a waveguide width of 7.5  $\mu\text{m}$ , where the 795 nm signal is down-converted to 1342 nm telecom O band.

The input and output end faces of the waveguides are anti-reflection (AR) coated for all wavelengths of interest to eliminate the Fresnel reflection loss. After fiber-pigtailling at the input end of the waveguides, the total waveguides throughputs are 70% and 60% for 795 nm and 1950 nm, respectively. A schematic diagram of our experimental setup is shown in Fig. S7b.

A single-frequency fiber laser manufactured by AdValue Photonics is used as the pump source, and 795 nm signal at the single-photon level is attenuated from continuous laser. As RPE lithium niobate waveguides support only TM-polarized modes, polarization controllers (PCs) are used to adjust the polarization for 795 nm and 1950 nm respectively. The working temperature of the waveguides is active stabilized by a thermoelectric cooling (TEC) system to maintain the phase-matching condition.

The down-converted photons and the remnant pump are collected with an AR-coated aspheric lens, and then the remnant pump is removed with two DMs ( $> 99.9\%$  reflectivity for 1342 nm and  $< 5\%$  reflectivity for 1950 nm). A long-pass filter edged at 1150 nm and a band-pass filter centered at 1342 nm with a bandwidth of 5 nm are used in combination to block the noises coming from the strong pump, including the spontaneous Raman scattering (SRS) noise and parasitic noise caused by imperfect periodic poling structure and second and third harmonic generation [4]. By the way, the amplifier spontaneous emission (ASE) from pump laser also contribute a lot around 1342 nm which has been cut off before entering the waveguide. When collecting the 1342 nm DFG signal into single-mode fiber, around 60% collection efficiency is achieved. Totally, the end-to-end efficiency of QFC module is 33%.

## V. IMPERFECTION OF PHOTON INTERFERENCE

In both SPI and TPI experiment, photon interference lies in the very heart of remote entanglement generation, which requires a good indistinguishability of photons from different ensembles. Hence we check it via Hong-Ou-Mandel (HOM) [5] experiment. As depicted in Fig. S8, we get HOM visibility  $V \equiv \frac{N_{min}}{2N_{average}}$  as 0.082 and 0.085 for write-out and read-out photon. Based on this, we calculate its influence to experiments. In the HOM experiment, two photons interference at the BS as:

$$a_A^\dagger b_B^\dagger \rightarrow (a_A^\dagger + ia_B^\dagger)(b_B^\dagger + ib_A^\dagger), \quad (\text{S17})$$

where  $a^\dagger$  and  $b^\dagger$  are creation operator of photon from different ensembles. We write the creation operator  $b^\dagger$  as the superposition of  $a^\dagger$  and  $\tilde{a}^\dagger$  (in the orthogonal space of  $a^\dagger$ ) as  $b^\dagger = \alpha a^\dagger + \beta \tilde{a}^\dagger$ . Then we get

$$a_A^\dagger b_B^\dagger \rightarrow \alpha(a_A^\dagger + ia_B^\dagger)(a_B^\dagger + ia_A^\dagger) + \beta(a_A^\dagger + ia_B^\dagger)(\tilde{a}_B^\dagger + i\tilde{a}_A^\dagger). \quad (\text{S18})$$

Item with coefficient  $\alpha$  represents perfect two-photon interference and contribute no coincidence. Item with coefficient  $\beta$  represent no interference and contribute coincidence with probability 1/2. Thus we can write HOM visibility as  $V_{HOM} = \frac{1}{2}\beta^2$ .

For TPI experiment, we characterize the inhomogeneity as a imperfect BSM measurement as

$$\hat{S}^\pm = (1 - \lambda) |\Psi_{pp}^\pm\rangle \langle \Psi_{pp}^\pm| + \lambda |\Psi_{pp}^\mp\rangle \langle \Psi_{pp}^\mp|. \quad (\text{S19})$$

Then the fidelity of remote atom-atom entanglement could be estimated as

$$\mathcal{F} = \text{Tr}[(|\Psi_{aa}^+\rangle \langle \Psi_{aa}^+|) \rho_{aa}^{AB}], \quad (\text{S20})$$

$$\rho_{aa}^{AB} = \text{Tr}_{pp}[(\mathbb{1}_{aa} \otimes \hat{S}) \rho_{ap}^A \rho_{ap}^B]. \quad (\text{S21})$$

To characterize  $\lambda$ , we write the bell state as

$$\begin{aligned} |\Psi^\pm\rangle &= a_E^\dagger b_L^\dagger \pm a_L^\dagger b_E^\dagger |vac\rangle \\ &= \left( \alpha(a_E^\dagger a_L^\dagger + a_L^\dagger a_E^\dagger) \pm \beta(a_E^\dagger \tilde{a}_L^\dagger + a_L^\dagger \tilde{a}_E^\dagger) \right) |vac\rangle. \end{aligned} \quad (\text{S22})$$

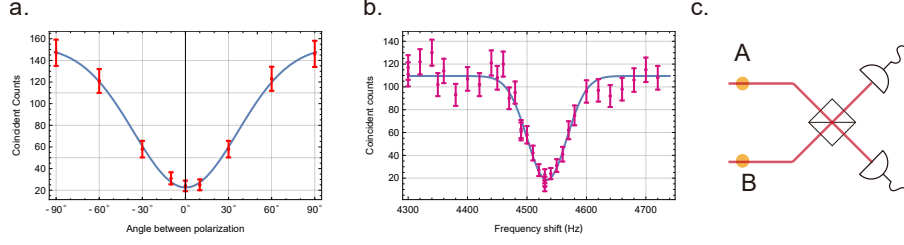


FIG. S8. Homogeneity of photons from different ensembles. a and b. Hon-Ou-Mandel results of write-out and read-out photon. c. Experimental setup.

The later item will contribute to two measurement result of BSM randomly, hence we get  $\lambda = \frac{1}{2}\beta^2$ . Note that the HOM result is also influenced by multiple photon, which is already counted when we perform tomography to  $\rho_A$  and  $\rho_B$ . So we amend HOM visibility by reducing its influence and get  $V'_{wo} = 0.063$ . We can calculate the result of S21 and get  $\mathcal{F} = 0.835$ , which is similar with experimental result  $\mathcal{F} = 0.842 \pm 0.080$ .

For SPI experiment, both write-out and read-out photon need to interfere. In entanglement creation process, two write-out optical fields from ensembles at Node-A and B need to interfere at a BS. Before the BS, we can write the state of two fields as

$$\begin{aligned} |\Psi\rangle &= (\mathbb{1} + \tilde{\chi}e^{i\theta}a_A^\dagger) \otimes (\mathbb{1} + \tilde{\chi}e^{i\theta'}b_B^\dagger) |vac\rangle \\ &= (\mathbb{1}\mathbb{1} + \tilde{\chi}e^{i\theta}a_A^\dagger\mathbb{1} + \tilde{\chi}e^{i\theta'}\mathbb{1}b_B^\dagger + \tilde{\chi}^2e^{i\theta+\theta'}a_A^\dagger b_B^\dagger) |vac\rangle, \end{aligned} \quad (S23)$$

where  $\tilde{\chi}$  is the reduced production probability including optical loss. Interference at BS as depicted in Fig. S8a will filter the first term of Eq. S23 and mix two middle terms together, which will herald two atomic ensembles entangled. Expanding  $b^\dagger$  in basis of  $a^\dagger$  and  $\tilde{a}^\dagger$ , we can write the evolution of two middle terms as

$$\begin{aligned} a_A^\dagger + e^{i\Delta\theta}b_B^\dagger &\rightarrow (a_A^\dagger + ia_B^\dagger) + e^{i\theta}(b_B^\dagger - ib_A^\dagger) \\ &= (1 + \alpha e^{i\theta})a_A^\dagger + i(1 - \alpha e^{i\theta})a_B^\dagger + \beta e^{i\theta}\tilde{a}_A^\dagger - i\beta e^{i\theta}\tilde{a}_B^\dagger. \end{aligned} \quad (S24)$$

When we setting  $\Delta\theta \equiv \theta - \theta' = 0$ , relative detection probability on detector A and B are

$$p_A = \frac{1}{4}(|1 - \alpha|^2 + \beta^2) = \frac{1 - \alpha}{2}, \quad p_B = \frac{1}{4}(|1 + \alpha|^2 + \beta^2) = \frac{1 + \alpha}{2} \quad (S25)$$

Based on this, Eq. S25 could be rewritten by  $V_{wo}$

$$p_A = \frac{1 - \sqrt{1 - 2V_{wo}^2}}{2}, \quad p_B = \frac{1 - \sqrt{1 + 2V_{wo}^2(0)}}{2} \quad (S26)$$

Similarly, in measurement  $\hat{\sigma}_\theta$ , two read-out fields will interfere as depicted in Fig. S3.

$$p_C = \frac{1 - \sqrt{1 - 2V_{ro}^2}}{2}, \quad p_D = \frac{1 - \sqrt{1 + 2V_{ro}^2}}{2} \quad (S27)$$

Among four combinations of detector coincidence  $\{aa', ab', ba', bb'\}$ , two of them is the max terms in deducing  $V_\theta$  and the other two is the min terms. Hence we can give a upper bound of  $V_\theta$  here using HOM results here as

$$V_\theta^{up} = \frac{max - min}{max + min} = p_C p_{C'} + p_D p_{D'} - p_C p_{D'} + p_D p_{C'} = 0.834. \quad (S28)$$

It is a little higher than  $V_\theta$  in QFC-free case, which means the main limit of  $V_\theta$  is from inhomogeneity of optical fields.

## VI. DEGRADATION OF $V_\theta$ IN LONG FIBER SITUATION

### A. Phase Instability

In long fiber situation, we probe the phase instability by monitoring the phase stabilizing laser. Through Gaussian fit, we deduce  $8.3^\circ$  and  $13.4^\circ$  fluctuation for 10 km and 50 km situation separately. Fig. S9 shows the statistic results

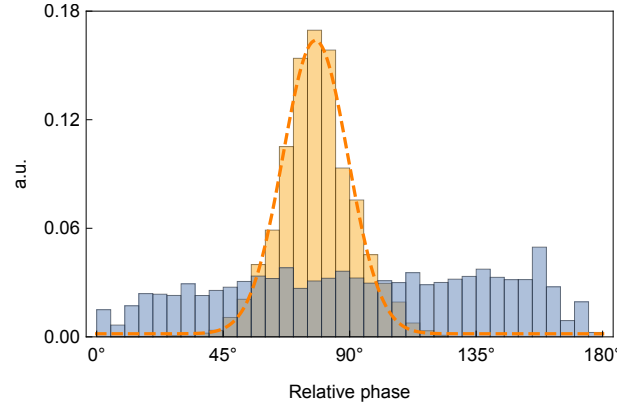


FIG. S9. Phase fluctuation of 50 km situation. Yellow bar correspond to stabilization and blue bar for not. Dashed curve fits the stabilized data.

of 50 km. Regarding phase fluctuation as a small disturb we consider disturbed state  $\rho'_{AB}$ , in which  $|\Psi^+\rangle$  and  $|\Psi^-\rangle$  are transferred to  $|\Psi_{\delta\theta}^+\rangle = |01\rangle + e^{i\delta\theta}|10\rangle$  and  $|\Psi_{\delta\theta}^-\rangle = |01\rangle - e^{i\delta\theta}|10\rangle$ . Take phase disturbance account, we have

$$\begin{aligned}
 V'_\theta &= \frac{\max' - \min'}{\max' + \min'} = \frac{\text{tr}(|\Psi^+\rangle\langle\Psi^+|\rho'_{AB}) - \text{tr}(|\Psi^-\rangle\langle\Psi^-|\rho'_{AB})}{\text{tr}(|\Psi^+\rangle\langle\Psi^+|\rho'_{AB}) + \text{tr}(|\Psi^-\rangle\langle\Psi^-|\rho'_{AB})} \\
 &= \frac{(c_+ - c_-) \cdot \int_{-\infty}^{+\infty} f(\delta\theta) \cos(\delta\theta) d\delta\theta}{c_+ + c_- + c_{11}} \\
 &= V_\theta \cdot C_{ph}.
 \end{aligned} \tag{S29}$$

$C_{ph} = \int_{-\infty}^{+\infty} f(\delta\theta) \cos(\delta\theta) d\delta\theta$  is a coefficient introduced by phase fluctuation, in which  $f(\delta\theta)$  is the Gaussian probability density function of phase distribution. Through calculation, we get  $C_{ph} = 0.989$  and  $0.973$  for 10 km and 50 km situation.

### B. Decrease of SNR

Along with write-out field being attenuated in long distance situation, dark counts of SNSPD introduce more disturbance. In 10 km and 50 km situation, we get about 15 : 1 and 4.5 : 1 counting ratio in SNSPD between with or without write-out field input. Considering definition of  $V_\theta \equiv (\max - \min)/(\max + \min)$ , random noise introduced will contribute to  $\max$  and  $\min$  term equally. Therefore, we have disturbed visibility

$$\begin{aligned}
 V'_\theta &= \frac{p_{\max} + p_{\text{noise}} - p_{\min} - p_{\text{noise}}}{p_{\max} + p_{\text{noise}} + p_{\min} + p_{\text{noise}}} \\
 &= V_\theta \cdot \frac{p_{\text{coin}}}{p_{\text{coin}} + p_{\text{noise}}}.
 \end{aligned} \tag{S30}$$

$p_{\text{noise}}$  correspond to probability of original coincidence, and  $p_{\text{noise}}$  correspond to the probability of coincidence newly introduced by dark counts. And we have

$$p_{\text{coin}} \approx 2\chi\eta_{\text{det}}^{SN}\eta_r\eta_{\text{det}}^{Si}, \quad p_{\text{noise}} \approx 2\frac{\chi\eta_{\text{det}}^{SN}}{SNR}p_a s\eta_{\text{det}}^{Si} \tag{S31}$$

After calculating, we know that  $V_\theta$  suffers 0.006 and 0.02 decrease for 10 km and 50 km situation.

### C. Mismatch of write-out fields

In entanglement building process, arriving time of write-out fields need to be calibrated same. We adjust difference of two optical paths length to achieve it. Via accumulating counts in SNSPD, we construct the shape of write-out fields and compare them. As depicted in Fig. S10, there exist 2.10 ns and 1.45 ns mismatch for 10 km and 50 km situation, which will bring  $5.8 \times 10^{-3}$  and  $3.0 \times 10^{-3}$  increase to  $V_\theta$  separately.

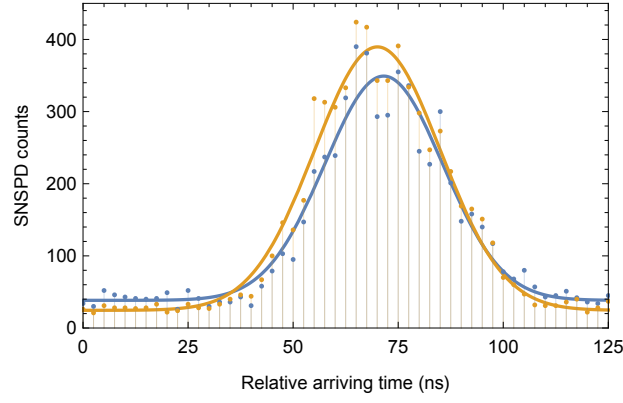


FIG. S10. Time domain waveform of write-out field from two different MOT. Dots for counts in SNSPD and curves for their fitting.

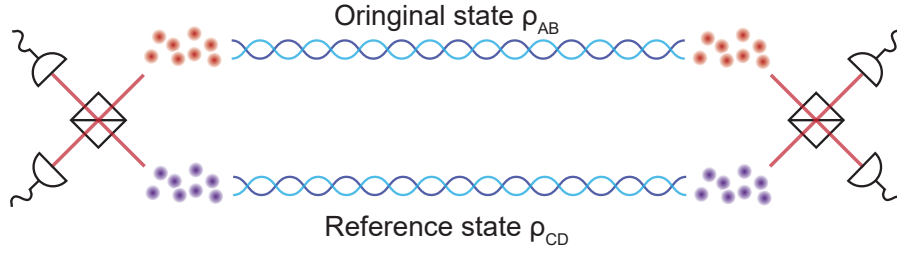


FIG. S11. Illustration of next step in DLCZ protocol.

## VII. FIDELITY ESTIMATION

In next step of DLCZ protocol, another EME state  $\rho_{CD}$  is introduced and lead to a PME state. Here we estimate the final Fidelity of this PME state. Four ensembles are retrieved into read-out fields simultaneously and two fields from one side are combined together by a BS. Through registering coincidence that only one detector clicks on each side, we capture PME state and perform communication. Consider this process and suppose an ideal state  $\rho_{CD} = |\Psi^+\rangle\langle\Psi^+|$  first for simplicity. Here we list four items of  $\rho_{AB} \otimes \rho_{CD}$  and their contribution in next step in Tab. S1.

TABLE S1. All combinations in PME preparation process with  $\rho_{AB}$  and  $|\Psi^+\rangle\langle\Psi^+|$ .

		$ 00\rangle$	$ \Psi^-\rangle$	$ \Psi^+\rangle$	$ 11\rangle$
Probability		$c_{00}$	$c_+$	$c_-$	$c_{11}$
Coef.	Right	0	1/2	0	1/2
	Wrong	0	0	1/2	1/2

Vacuum part contribute nothing to final results due to no coincidence it gives. Coefficient 1/2 from  $|\Psi^+\rangle$  is a intrinsic success probability of this protocol. Because of converse phase,  $|\Psi^-\rangle$  give rise to false coincidences. Owing to two read-out fields exist at the same time,  $|11\rangle$  always gives coincidence. And it contribute equally to right and wrong part thanks to randomness. We calculate the fidelity of PME state as

$$\mathcal{F}_{\rho,+} = \frac{Right}{Right + Wrong} = \frac{c_+ + c_{11}}{c_+ + c_- + 2c_{11}} \quad (S32)$$

Comparing expression of  $\mathcal{F}_{post} = \frac{c_+}{c_+ + c_- + c_{11}}$ , because  $c_{11} \ll c_+, c_-$ , we have  $\mathcal{F}_{post} \approx \mathcal{F}_{\rho,+}$ . Considering more realistic situation that  $\rho_{CD} = \rho_{AB}$ . We list all outputs in Tab. S2. Then the fidelity of PME state could be calculate similar

$$\mathcal{F}_{\rho,\rho} = \frac{Right}{Right + Wrong} \approx \frac{1}{2} [1 + V_\theta^2 (1 + V_F^2)] \quad (S33)$$



TABLE S2. All combinations in PME preparation process with two  $\rho_{AB}$ .

		$ 00\rangle$	$ 00\rangle$	$ 00\rangle$	$ 00\rangle$	$ \Psi^+\rangle$	$ \Psi^+\rangle$	$ \Psi^+\rangle$	$ \Psi^+\rangle$	$ \Psi^-\rangle$	$ \Psi^-\rangle$	$ \Psi^-\rangle$	$ \Psi^-\rangle$	$ 11\rangle$	$ 11\rangle$	$ 11\rangle$	$ 11\rangle$
		$ 00\rangle$	$ \Psi^+\rangle$	$ \Psi^-\rangle$	$ 11\rangle$	$ 00\rangle$	$ \Psi^+\rangle$	$ \Psi^-\rangle$	$ 11\rangle$	$ 00\rangle$	$ \Psi^+\rangle$	$ \Psi^-\rangle$	$ 11\rangle$	$ 00\rangle$	$ \Psi^+\rangle$	$ \Psi^-\rangle$	$ 11\rangle$
Probability		$c_{00}c_{00}$	$c_{00}c_{+}$	$c_{00}c_{-}$	$c_{00}c_{11}$	$c_{+}c_{00}$	$c_{+}c_{+}$	$c_{+}c_{-}$	$c_{+}c_{11}$	$c_{-}c_{00}$	$c_{-}c_{+}$	$c_{-}c_{-}$	$c_{-}c_{11}$	$c_{11}c_{00}$	$c_{11}c_{+}$	$c_{11}c_{-}$	$c_{11}c_{11}$
Coef.	Right	0	0	0	1/2	0	1/2	0	1/2	0	0	1/2	1/2	1/2	1/2	1/2	1/2
	Wrong	0	0	0	1/2	0	0	1/2	1/2	0	1/2	0	1/2	1/2	1/2	1/2	1/2

TABLE S3. Comparison of fidelity from two methods.

	$\mathcal{F}_{post}$	$\mathcal{F}_{\rho,+}$	$\mathcal{F}_{\rho,\rho}$
Not conv./ 5 m	0.896	0.899	0.789
Conv./ 10 m	0.900	0.901	0.806
Conv./ 10 km	0.842	0.844	0.724
Conv./ 50 km	0.832	0.834	0.709

Still, we show all simulation results in Tab. S3.

- 
- [1] Parameswaran, K. R. *et al.* Highly efficient second-harmonic generation in buried waveguides formed by annealed and reverse proton exchange in periodically poled lithium niobate. *Optics Letters* **27**, 179–181 (2002).
  - [2] Roussev, R. V., Langrock, C., Kurz, J. R. & Fejer, M. Periodically poled lithium niobate waveguide sum-frequency generator for efficient single-photon detection at communication wavelengths. *Optics Letters* **29**, 1518–1520 (2004).
  - [3] Chou, M., Hauden, J., Arbore, M. & Fejer, M. 1.5- $\mu$ m-band wavelength conversion based on difference-frequency generation in linbo 3 waveguides with integrated coupling structures. *Optics Letters* **23**, 1004–1006 (1998).
  - [4] Pelc, J. S. *et al.* Long-wavelength-pumped upconversion single-photon detector at 1550 nm: performance and noise analysis. *Optics Express* **19**, 21445–21456 (2011).
  - [5] Hong, C.-K., Ou, Z.-Y. & Mandel, L. Measurement of subpicosecond time intervals between two photons by interference. *Physical Review Letters* **59**, 2044 (1987).